frontiers | Frontiers in Earth Science

TYPE Original Research
PUBLISHED 11 January 2023
DOI 10.3389/feart.2022.1083799

OPEN ACCESS

EDITED BY
Shihua Zhong,
Ocean University of China, China

REVIEWED BY
Hua-Wen Cao,
China Geological Survey, China
Jianming Zhu,
China University of Geosciences, China

*CORRESPONDENCE
Yi-Qu Xiong,
xiongyiqu@126.com
Han-Tao Wei,
654095322@qq.com

SPECIALTY SECTION
This article was submitted to Geochemistry, a section of the journal Frontiers in Earth Science

RECEIVED 29 October 2022
ACCEPTED 30 December 2022
PUBLISHED 11 January 2023

CITATION
Tan R-C, Shao Y-J, Wei H-T, Zhang J-K, Yu M-D and Xiong Y-Q (2023), Hydrothermal fluid characteristics of the huayuan Pb-Zn orefield: Constraints from apatite major and trace element compositions.
Front. Earth Sci. 10:1083799.
doi: 10.3389/feart.2022.1083799

Hydrothermal fluid characteristics of the huayuan Pb-Zn orefield: Constraints from apatite major and trace element compositions

Rui-Chang Tan[1,2,3], Yong-Jun Shao[1,3], Han-Tao Wei[1,4]*, Jun-Ke Zhang[1,3], Meng-Da Yu[1,3] and Yi-Qu Xiong[1,3]*

[1]School of Geosciences and Info-Physics, Central South University, Changsha, China, [2]Hunan Key Laboratory of Land Resources Evaluation and Utilization, Changsha, China, [3]Key Laboratory of Metallogenic Prediction of Nonferrous Metals and Geological Environment Monitoring, Ministry of Education, School of Geosciences and Info-Physics, Central South University, Changsha, China, [4]Development Research Center, China Geological Survey, Beijing, China

The Huayuan orefield in the SW Yangtze Block (SW China) is a world-class Pb-Zn orefield, with over 20 million tonnes (Mt) metal reserve. However, the Pb-Zn ore fluid source and evolution in Huayuan remain controversial. This study determined the major and trace element compositions of the newly-identified apatite from the Pb-Zn ores, using electron microprobe analysis (EMPA) and laser ablation inductively coupled plasma mass spectrometry (LA-ICP-MS). The apatite samples are of hydrothermal origin, and have high CaO (52.57–57.15 wt%), P_2O_5 (39.26–42.88 wt %) and F (1.82–3.90 wt%) but low Cl (< 0.42 wt%) contents. The samples have total rare Earth element content (ΣREE) of 74.07–1,255.34 ppm, and they all show negative Eu and weakly positive Ce anomalies. The result suggests that the apatite was formed in an environment with decreasing oxygen fugacity, and in relatively F-rich, Cl-poor, and REE-poor ore-forming fluid. We geochemically compared the apatite from Huayuan with those from different geneses by Fisher discriminant. The result suggests that the Huayuan apatite is distinct from typical magmatic and purely hydrothermal apatite, and that the ore-forming fluids may have had multiple sources. The mixing of fluids with different origins may have triggered significant metal ore deposition.

KEYWORDS

apatite, major elements, trace elements, fluid evolution, Fisher discriminant

1 Introduction

The Huayuan orefield, containing approximately 300 Pb-Zn deposits with over 20 million tonnes (Mt) of Pb-Zn reserve (Zhao et al., 2016; Li, 2018), is a world-class carbonate-hosted Pb-Zn orefield (Shu, 1983; Xie, 1983; Zhou et al., 1983; Sun et al., 1985; Peng, 1986; Wei et al., 2017). The Huayuan Pb-Zn deposits have simple ore mineralogy, and are characterized by large tonnage low-grade ores (avg. 4% Pb + Zn) (Wei et al., 2020). The ores are hosted by the Lower Cambrian Qingxudong Fm. (LCQF) carbonate rocks, and the ore-forming fluids have low-medium temperature (140°C–220°C) and medium-high salinity (11.0–19.0 wt% NaCleqv) (Liu and Zheng, 1999; Cai et al., 2014; Duan et al., 2014; Wei et al., 2017). Bitumen and methane are found in fluid inclusions (Liu et al., 1999; Zhou et al., 2014), and the dominant mineralization is interpreted to be thermochemical sulfate reduction (TSR) related (Zhou et al., 2014; Wei et al., 2017). The basement clastic rocks are considered as the primary metal source (Yang et al., 2022; Zhang et al., 2022).

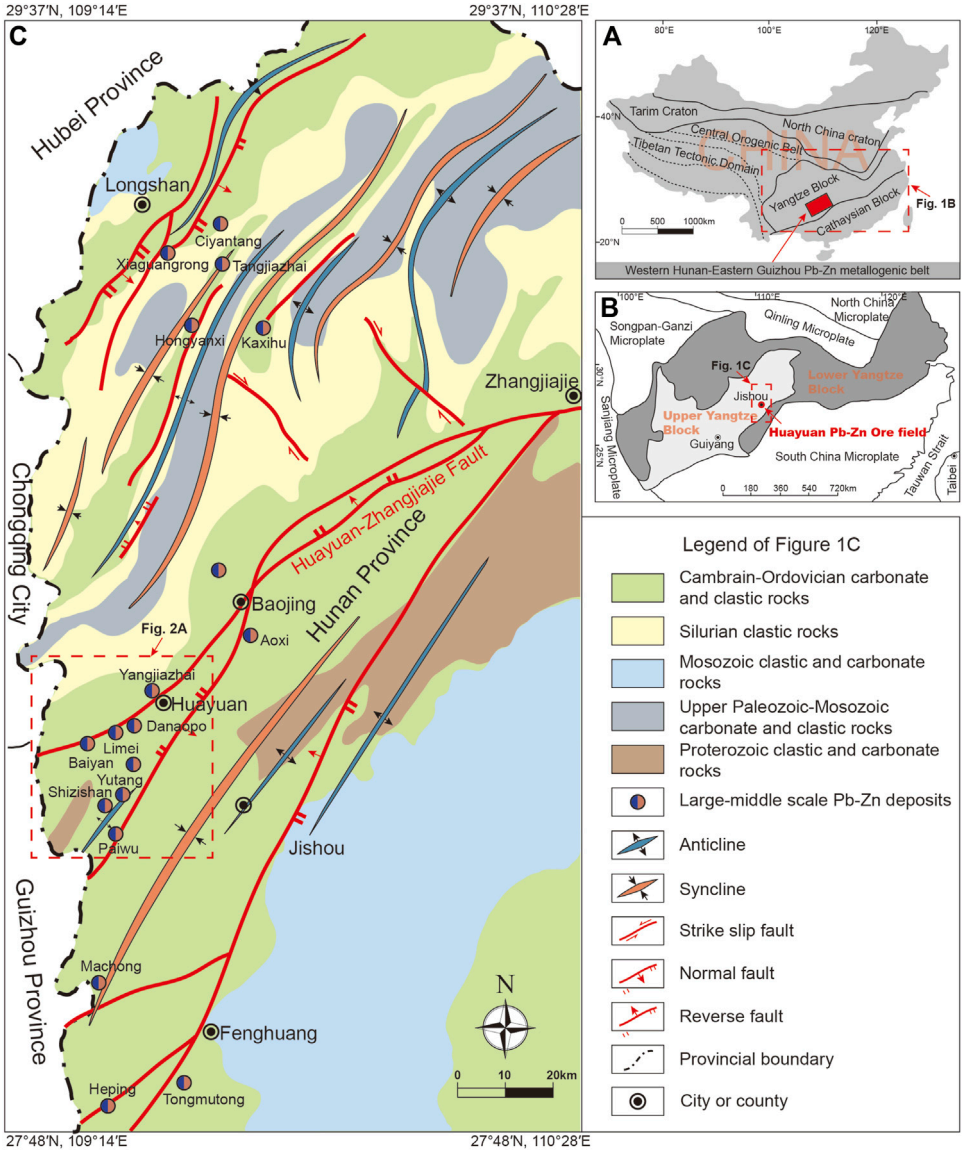

FIGURE 1
(A) Regional tectonic map of the western Hunan-eastern Guizhou Pb-Zn metallogenic belt (modified after Zhou et al., 2013; Wu et al., 2021); **(B)** Geotectonic map of the Huayuan Pb-Zn orefield in the Upper Yangtze Block (modified after Wu et al., 2021). **(C)** Geologic map of the Western Hunan Pb-Zn metallogenic belt in South China (modified after Wu et al., 2021; Yang and Lao, 2007) showing the distribution of Pb-Zn deposits, structures, and strata.

In terms of the ore-fluid origin, some authors proposed a formation water source (Zhou et al., 2014; 2017), whereas some others preferred a deeper origin (Wei et al., 2017; Wu et al., 2021). Hydrothermal apatite, a resistate accessory mineral suitable for geochemical and geochronological analyses (Hassan et al., 1977; Kordian et al., 2020; Wang et al., 2022), could provide new clues for the fluid source(s) and evolution (McClellan and Van Kauwenbergh, 1990; Ayers and Watson, 1993; Prokopyev et al., 2017; Hu et al., 2019). In recent years, *in situ* microanalysis on accessory minerals (incl. apatite) is increasingly used to determine the evolution of magmatic-hydrothermal activity and the mineralization age (Barfod et al., 2005; Edfelt et al., 2005; Deng et al., 2015; Kusebauch et al., 2015; Pan et al., 2016; Xu et al., 2019). In this study, we have newly discovered apatite from the Huayuan Pb-Zn orefield, and have analyzed their geochemical compositions (*via* EMPA and LA-ICP-MS) to trace the ore-material source(s) and the hydrothermal evolution. We also compared our data with an apatite database. The Fisher discrimination analysis was also conducted to classify the genetic type of apatite from Huayuan.

2 Regional geology

The Yangtze Block is bounded by the Qinling, Sanjiang, Songpan–Ganze, and Cathaysia terranes/fold-belts to the north, west, northwest, and southwest, respectively (Figures 1A, B). It comprises a late Paleoproterozoic-early Neoproterozoic crystalline basement of meta-sandstone/-siltstone and silty slate, covered by Upper Ediacaran to Quaternary sedimentary sequences (Metcalfe,

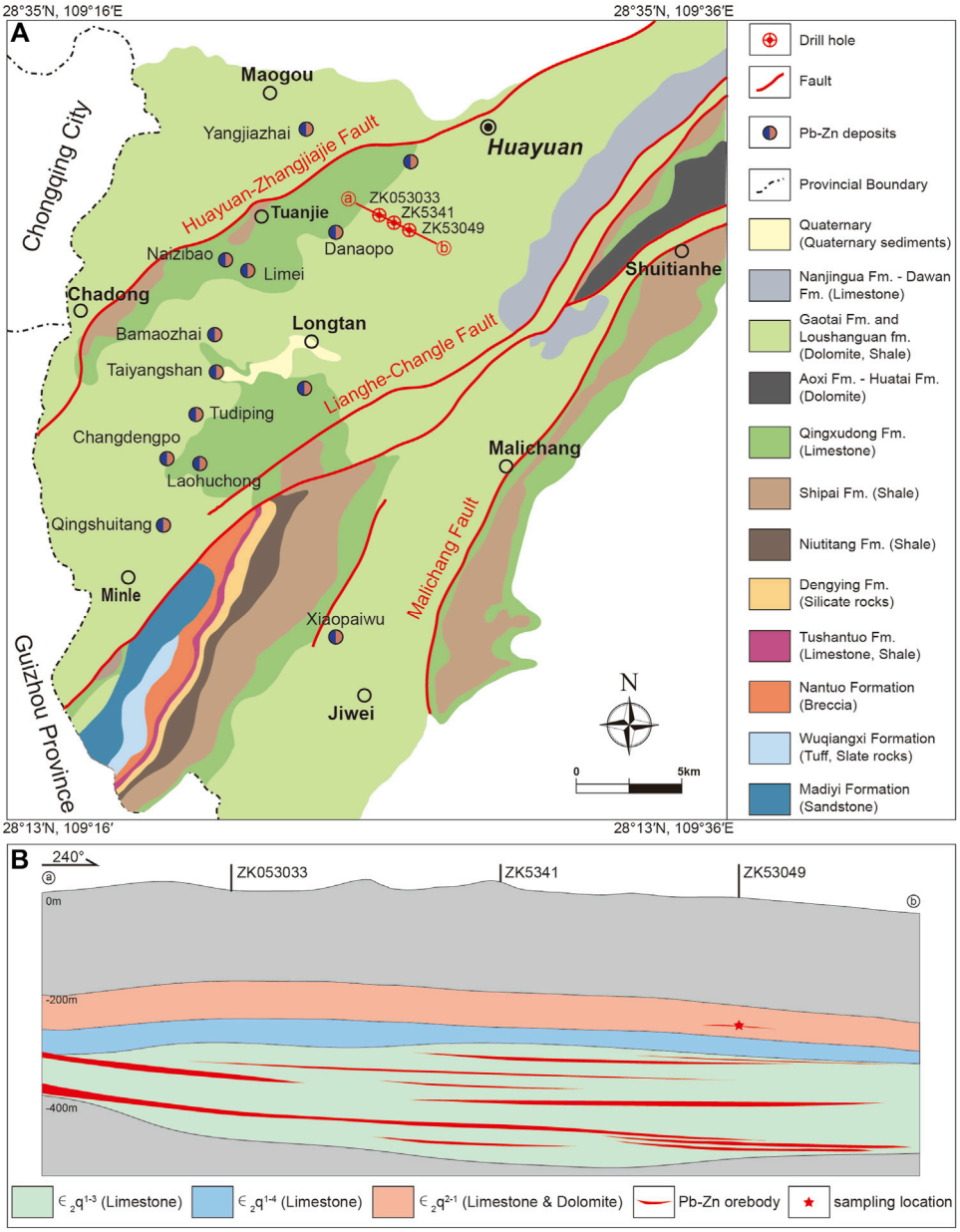

FIGURE 2
(A) Geological map of the Huayuan Pb-Zn orefield (modified after Duan, 2014). **(B)** Geological profile of the Danaopo Exploration Line No. 53.

2006; Hu et al., 2022). Regional magmatism was minor and largely ore-unrelated (Yang and Lao, 2007; Duan et al., 2014). The Yangtze Block has undergone multiple tectonic events (Metcalfe, 2006; Charvet, 2013): 1) 850 to 820 Ma: the Yangtze Block and Cathaysia Block were amalgamated along the Jiangnan suture (e.g., Zhao et al., 2011); 2) after ~820 Ma, Neoproterozoic to Ordovician deep-water sedimentary rocks were deposited in central South China along a failed Neoproterozoic intracontinental rift (i.e., the Nanhua rift) (e.g., Wang and Li, 2003). During the intracontinental Wuyi-Yunkai orogeny (490–410 Ma), the Nanhua rift had evolved into a foreland basin (Yao and Li, 2016). In the Early Triassic, the South China-North China collision occurred along the Qingling-Dabie Orogen, and the Cimmerian continental ribbons (incl. Indochina and Sibumasu) were accreted onto the southwestern South China margin (e.g., Metcalfe, 2006). The NE-trending Huangyuan–Zhangjiajie regional fault zone controlled the distribution of Pb-Zn deposits in the Xiangxi–Qiandong metallogenic belt (XQMB) (Figures 1C; Figure 2) (Li et al., 2010).

3 Orefield geology

3.1 Stratigraphy

Exposed strata in Huayuan comprises the metamorphosed basement made of the Banxi Group meta-sandstone/-siltstone and silty slate, the Upper Ediacaran Dengying Formation (Fm.) cherty dolostone, and the Lower-Middle Cambrian to Ordovician clastic and

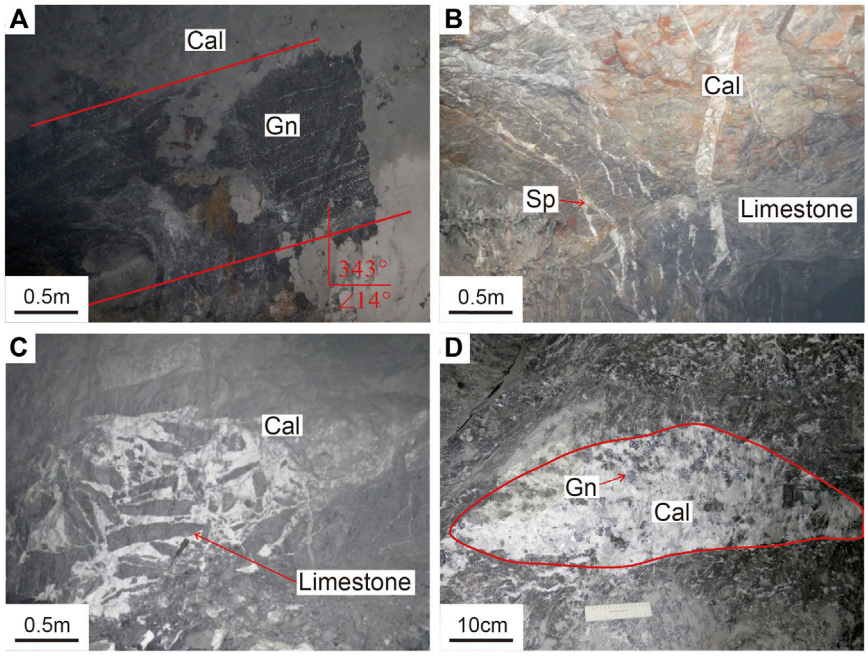

FIGURE 3
Different types of orebodies in the Huayuan Pb-Zn orefield: **(A)** layered, **(B)** veined, **(C)** breccia, and **(D)** lenticular orebody.

carbonate rocks (Figure 2). The Pb-Zn sulfide ores occur in the reef zones of carbonate platform facies, particularly the LCQF reef limestone (Tang et al., 2012). The Qingxudong Formation comprises a lower member (mainly argillaceous/dolomitic/algal limestone) and upper member (mainly argillaceous/micritic dolomite) (e.g., Wu et al., 2021). Magmatic rocks are rarely distributed in the district.

3.2 Structures

Faults are well developed and controlled the Pb-Zn orebody distribution in the Huayuan orefield (Figure 2). These faults are dominantly NE- and NNE-trending, including the Huayuan-Zhangjiajie (dip angle: 60°–75°), Lianghe-Changle (dip angle: 25°–30°), and the Malichang (dip angle: 40°–60°). Among them, the Huayuan-Zhangjiajie fault is the main ore-controlling structure. Open-space structures (incl. Pores, joints, and stylolites) developed in the carbonate rocks may have served as the ore deposition sites in the Huayuan Pb-Zn orefield (Fu, 2011).

3.3 Orebodies

Major deposits in the Huayuan orefield include the Danaopo (4.5 Mt), Qingshuitang (2.9 Mt), Limei (3.0 Mt), and the Yutang (3.5 Mt). Four types of orebodies were recognized in the orefield (Figure 3): 1) stratiform replacement type is widespread and accounts for 80% of the total Pb + Zn reserve (ore grade: 3% Zn + Pb). The orebodies dip gently to the SE (dip angle: 2°–12°); 2) vein type is strictly controlled by NE-trending faults (ore grade: >10% Pb + Zn), distributed mainly in the northern Huayuan orefield with dip angle of 30°–50°; 3) breccia type is only distributed in the third bed of the LCQF lower member, and is commonly by high grade (ore grade: >25% Pb + Zn); iv) lenticular type is distributed in the third-fourth bed of the LCQF lower member, and is usually multilayered (commonly three to seven layers; ore grade: 4–10% Pb + Zn).

3.4 Alteration and mineralization paragenesis

The Huayuan Pb-Zn orefield contains both oxide and sulfide ores, with metallic minerals including mainly sphalerite, galena, and pyrite (Figure 4), and non-metallic minerals including mainly calcite, dolomite, barite, and fluorite. Ore textures include vein (Figure 4A), disseminated (Figure 4E), metasomatic (Figure 5I), poikilitic (Figures 5A,F,I), and cataclastic (Figure 5I). The alteration can be divided into the diagenetic, hydrothermal, and supergene periods (Wu et al., 2021), with the hydrothermal period further divided into three stages: (early-ore Ⅰ) calcite + dolomite + fluorite + pyrite + sphalerite; (main-ore Ⅱ) calcite + dolomite + barite + pyrite + sphalerite + galena; and (late-ore Ⅲ) calcite + sphalerite + galena.

3.5 Petrography characteristic of apatite samples

The apatite samples were collected from recrystallized limestone in the lower part of LCQF. Pyrite, sphalerite, barite, and apatite were deposited in the holes formed by dissolution and recrystallization. Apatite grains are scattered around sphalerite, and are euhedral hexagonal to anhedral granular, with sizes of 20–60 μm (Figure 5). Some apatite grains contain pyrite and zircon inclusions (Figures 5F,G,I). Euhedral apatite has a flat smooth

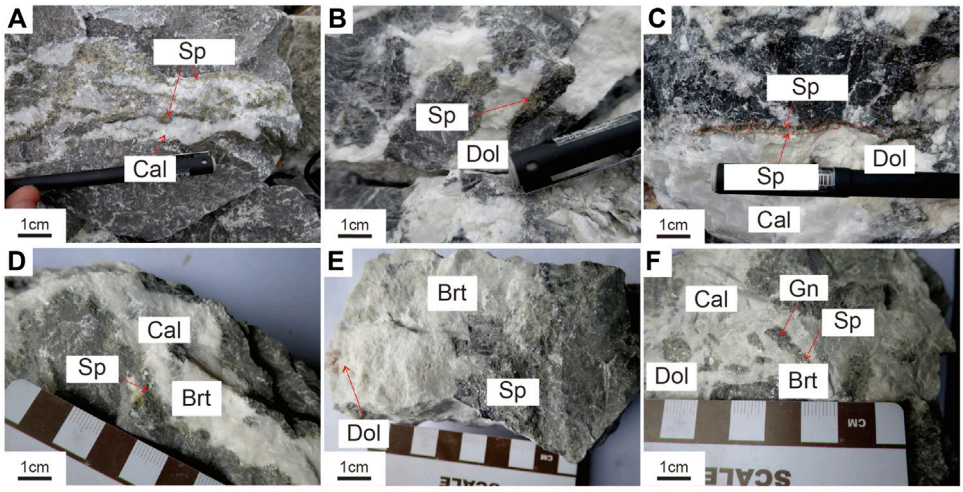

FIGURE 4
Photos of ore types in the Huayuan Pb-Zn orefield.

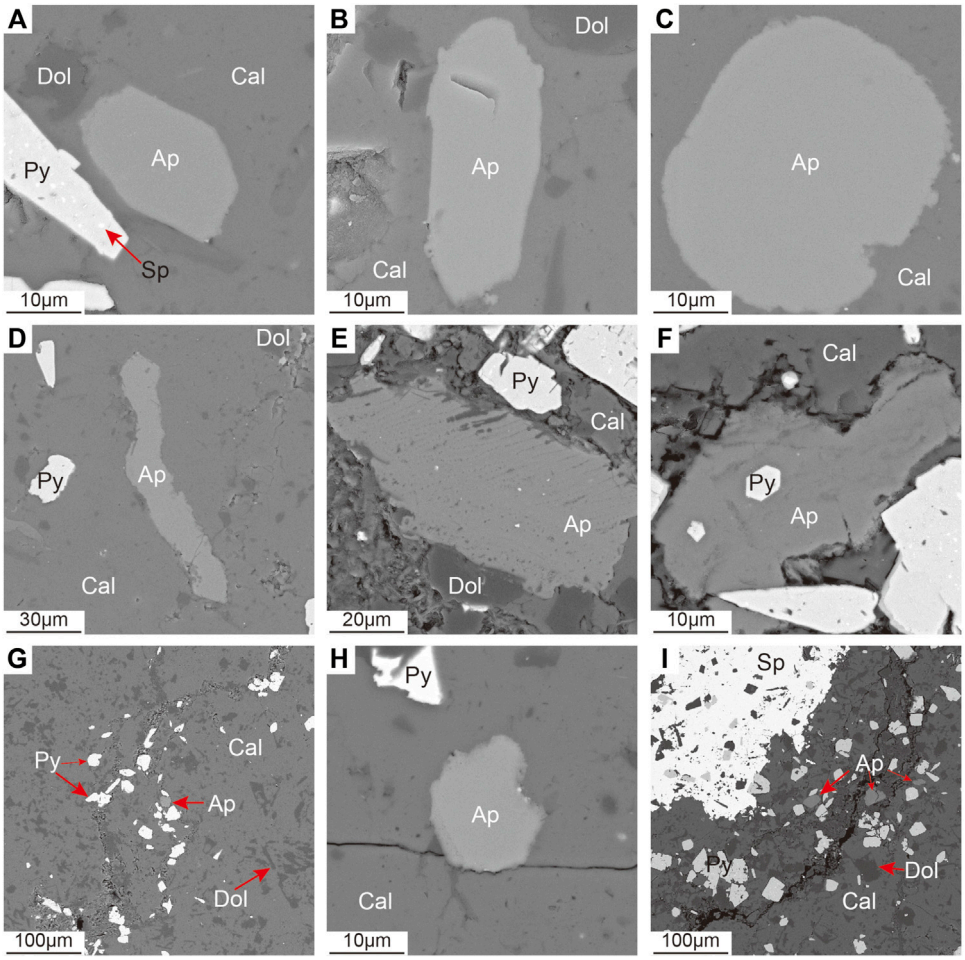

FIGURE 5
Back-scattered electron (BSE) photographs of apatite from the Huayuan Pb-Zn orefield: **(A)** automorphic apatite; **(B)** hypidiomorphic apatite; **(C)** xenomorphic apatite; **(D)** xenomorphic apatite with flow structure; **(E)** hypidiomorphic-xenomorphic apatite with numerous fluid inclusions; **(F)** pyrite inclusions in apatite; **(G)** apatite in veins with pyrite; **(H)** apatite cutting fissures formed by diagenesis; and **(I)** apatite and pyrite distributed around sphalerite.

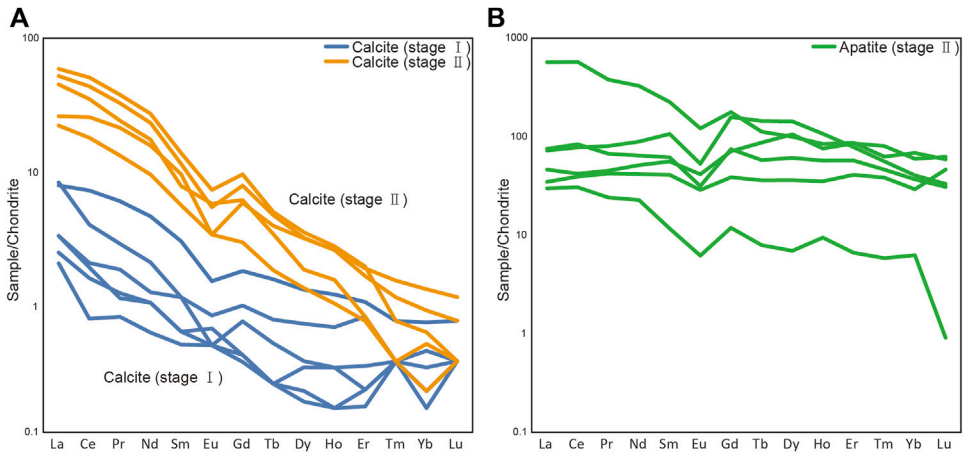

FIGURE 6
Chondrite-normalized REE patterns of **(A)** calcite (after Wei et al., 2017); **(B)** apatite from the Huayuan Pb-Zn orefield.

surface and lacks impurities or fluid inclusions. Anhedral apatite has many fluid inclusions.

4 Sampling and analytical methods

4.1 Sampling

Stage II disseminated pyrite-sphalerite ore samples were collected from the Danaopo deposit (drill-hole ZK53049, 265–229 m depth, 109°28′E, 28°29′N). Eighteen polished thin-sections were prepared and observed under the optical microscope and SEM to determine the mineral paragenesis. Eight apatite-bearing samples were selected for *in-situ* major and trace element analyses.

4.2 EPMA major and minor element analysis

The analysis was conducted on a JEOL JXA-8230 Electron Probe Microanalyzer equipped with five wavelength-dispersive spectrometers (WDS), at the Laboratory of Microscopy and Microanalysis, Wuhan Microbeam Analysis Technology Co. Ltd. The samples were first carbon-coated, with the precautions (suggested by Zhang and Yang, 2016) taken to minimize the difference of carbon film thickness between samples and obtain a largely uniform (~20 nm thick) coating (Zhang and Yang, 2016). Details of the EPMA procedures are described in Yang et al. (2022). Operating conditions for quantitative WDS analyses include 15 kV accelerating voltage, 5 nA beam current, and 5 μm spot size. Data were corrected online using the ZAF (atomic number, absorption, fluorescence) correction procedure. The peak counting time is 10 s for Ca, S, P, Cl. F, Si, Sr, Mg, Na, Zn, Cu, Fe and 20 s for Mn and Ti. The background counting time is half of the peak counting time on the high- and low-energy background positions. The following standards were used: Apatite (P, Ca), Barium fluoride (F), Halite (Cl), Pyrite (S), Olivine (Si), Jadeite (Na), Pyrope garnet (Fe), Strontium fluoride (Sr), Rhodonite (Mn), Rutile (Ti), Cuprum (Cu), Zinc (Zn), and Diopside (Mg).

4.3 LA-ICP-MS trace element analysis

The analysis was performed at the Key Laboratory of Metallogenic Prediction of Non-ferrous Metals and Geological Environment Monitoring (Central South University), Ministry of Education. The analysis used a Telydyne Cetac HE 193 nm laser ablation system, coupled with an Analytik Jena PlasmaQuant MS Elite plasma mass spectrometer. The National Institute of Standards and Technology (NIST) standard SRM610 was used as the external standard, Ca as the

TABLE 1 Fisher discriminant predictive classification, based on major element concentrations.

	Predictive classification					
Ture Classification	Hydrothermal			Magmatic	Huayuan	Total
	Count	Hydrothermal	22	8	0	30
		Magmatic	115	184	63	362
		Huayuan	5	5	46	56
	%	Hydrothermal	73.3	26.7	0.0	100.0
		Magmatic	31.8	50.8	17.4	100.0
		Huayuan	8.9	8.9	82.1	100.0

TABLE 2 Fisher discriminant predictive classification, based on trace element concentrations.

	Predictive classification					
Ture Classification	Hydrothermal			Magmatic	Huayuan	Total
	Count	Hydrothermal	23	0	0	23
		Magmatic	0	94	17	111
		Huayuan	0	0	6	6
	%	Hydrothermal	100.0	0.0	0.0	100.0
		Magmatic	0.0	84.7	15.3	100.0
		Huayuan	0.0	0.0	100.0	100.0

internal standard, standard GSE-2G as the other standard, and NIST SRM612 for signal correction during the analyses. The analytical conditions include 3.5 J/cm^2 energy density, 15 μm beam spot size, 5 Hz frequency, 13.5 L/min Ar gas flow, and 1.1 L/min He flow. The apatite ablation time of 70 s, comprising 20 s background measurement, 30 s sample signal measurement, and 20 s for washing. The instrument tuning conditions are as follows: NIST SRM 610 206 Pb and 232Th contents > 600,000 counts; 248ThO/232Th < 3‰; 206 Pb/238U = .20–.25; 232Th/238U = .95–1.05. The elements measured include Sc, Ti, Ga, Rb, Sr, Y, Zr, Nb, Mo, Sn, Ba, La, Ce, Pr, Nd, Sm, Eu, Gd, Tb, Dy, Ho, Tm, Yb, Lu, Hf, Ta, Pb, Th, and U. The detection limit and analytical errors are listed in Supplementary Table S2.

4.4 Fisher discriminant analysis

Fisher discriminant analysis is a linear dimensionality reduction technique that maximizes the separation between several classes (Duda and Hart, 1973). We performed the Fisher discrimination on the compiled apatite data in python. A short mathematical description follows.

Stacking the training data for all classes into a n by m matrix X and representing the ith row of X with the column vector x_i, the total-scatter matrix is

$$S_t = \sum_{i=1}^{n} (x_i - x_{mean})(x_i - x_{mean})^T, \quad (1)$$

where x_{mean} is the total mean vector whose elements correspond to the means of the columns of X. Define X_j as the set of vectors x_i which belong to the class j, the within-scatter matrix for class j is

$$S_j = \sum_{x_i \in X_j}^{n} (x_i - x_{j,mean})(x_i - x_{j,mean})^T, \quad (2)$$

where $x_{j,mean}$ is the mean vector for class j. Let c be the number of classes, then

$$S_W = \sum_{i=1}^{c} S_i, \quad (3)$$

is the within-class-scatter matrix, and

$$S_b = \sum_{j=1}^{c} n_j (x_{j,mean} - x_{mean})(x_{j,mean} - x_{mean})^T, \quad (4)$$

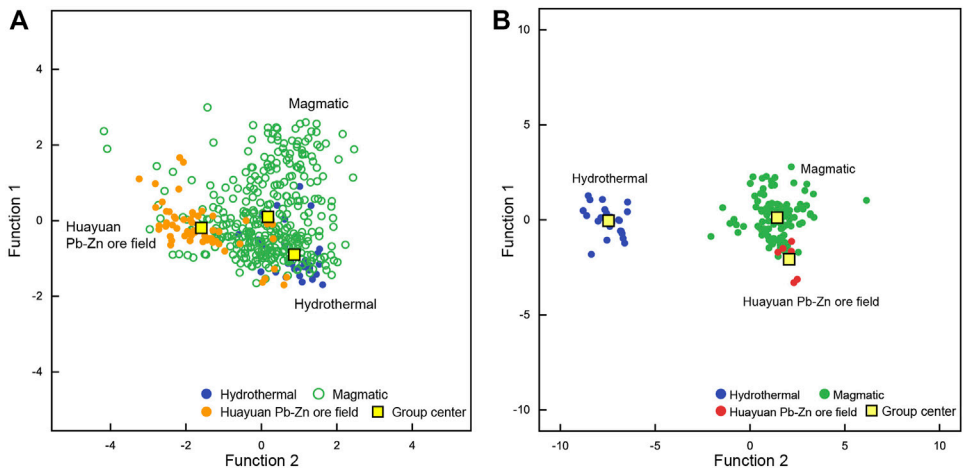

FIGURE 7
Classification plots based on **(A)** major element and **(B)** trace element concentrations.

is the between-class-scatter matrix where n_j is the number of observations in class j.

The first FDA vector w_1 can be determined as

$$\max_{w_1} \frac{w_1^T S_b w_1}{w_1^T S_W w_1}. \quad (5)$$

The second FDA vector is computed so as to maximize the scatter between classes while minimizing the scatter within classes among all axes perpendicular to the first FDA vector, and so on for the remaining FDA vectors. It can be shown mathematically that FDA vectors are equal to the eigenvectors w_k of the generalized eigenvalue problem

$$S_b w_k = \lambda_j S_W w_k, \quad (6)$$

where the eigenvalues λ_k indicate the degree of overall separability among the classes by projecting the data onto w_k. With FDA vectors determined, observations are then classified in this reduced FDA space using discriminant analysis (Duda and Hart, 1973; Chiang et al., 2000; 2004; Hastie et al., 2009).

5 Analytical results

5.1 Major element composition

The apatite samples have high CaO (52.57–57.15 wt%, mean 54.62 wt%, n = 90), P_2O_5 (39.26–42.88 wt%, mean 41.18 wt%, n = 90), and F (1.82–3.90 wt%, mean 2.92 wt%, n = 90) concentrations. The Cl content is low (<.42 wt%, mean .085 wt%, n = 90), with that of some samples below the detection limit. The Fe content is .02–.53 wt% (mean .19 wt%, n = 90). The maximum Na_2O, MgO, SiO_2, SO_3, MnO, and SrO contents are .40 wt%, .74 wt%, 1.3 wt%, .89 wt%, .54 wt%, and .40 wt%, respectively (Supplementary Table S1).

5.2 Trace element compositions

The apatite samples are characterized by elevated total rare Earth element concentrations (ΣREE = 74.07–1,255.34 ppm, avg. 388.09 ppm, n = 6). The concentrations of total light and heavy REEs (LREEs and HREEs) are of 63.06–1,106.44 ppm (avg. 294.80 ppm, n = 6) and 11.01–153.05 ppm (avg. 93.29 ppm, n = 6), respectively. Except for samples DZK114J-4–1 (ΣLREE/ΣHREE = 5.73) and DZK114J-9–2 (ΣLREE/ΣHREE = 7.43), the ΣLREE/ΣHREE of the most apatite samples are 1.02–2.23 (avg. 1.62, n = 4) (Supplementary Table S2).

The samples have gentle chondrite-normalized REE patterns (Figure 6B) and distinct negative Eu_N anomalies (Eu/Eu* = .40–.72, avg. .56, n = 6). All samples show weakly positive Ce_N anomalies (Ce/Ce* = .92–1.21, avg. 1.08, n = 6) and a narrow Y/Ho range (10.47–13.53, avg. 12.65, n = 6).

The Huayuan apatite are characterized by high Th (10.71–46.42 ppm) and U (1.12–74.29 ppm) concentrations. Except for sample DZK114J-4–1 (Th/U = .14), the Th/U ratio of most apatite samples is 3.55–24.01 (avg. 10.06, n = 5). The Hf, Zr, Ta, W, and Nb concentrations are low (albeit above the detection limits), with maximum values of 1.65 ppm, 3.9 ppm, 10.82 ppm, 7.16 ppm, and 4.28 ppm, respectively.

5.3 Genetic classification of apatite

Fisher discriminant analysis was conducted on the new and published apatite data, based on seven major and 14 trace elements (O'Sullivan et al., 2020), to define a discrimination model for the different types of apatite. Accordingly, 56.3% and 87.9% of the original classified samples are correctly classified, respectively (Tables 1, 2). In the Fisher discriminant plot (Figure 7), the horizontal and vertical axes represent the values of the two canonical discriminant functions. The plot shows clear clustering of data for apatite from the different origins (hydrothermal, magmatic, and the Huayuan Pb-Zn orefield).

6 Discussion

6.1 Genesis of apatite

The general chemical formula for apatite is $A_{10}(PO_4)_6Z_2$, and the standard chemical formula is $Ca_5(PO_4)_3$(F, Cl, OH). The A position is mainly a divalent cation dominated by Ca^{2+}, and the Z position is usually an anion, such as F^-, OH^-, or Cl^- (Griffin, 2008). The calcium ions have coordination numbers 7 and 9 (Hughes and Rakovan, 2018): the former is linked to nine oxygen atoms, whilst the latter is linked to one Z ion and six oxygen atoms. Various ions, such as Sr^{2+}, Pb^{2+}, Mg^{2+}, Na^+, and Fe^{2+}, can replace the Ca^{2+} through isomorphism.

Apatite has commonly three major origins, i.e., magmatic, hydrothermal, and tuff (Sha and Chappell, 1999). The Huayuan apatite has much lower ΣREE (74–1,255 ppm, mean 388 ppm, n = 6) than that of typical magmatic apatite, but higher than that of apatite in tuff (Zhu et al., 2004). Therefore, the Huayuan apatite may have had a hydrothermal fluid source. Some apatite samples have pores, fluid inclusions, and flow structures. These pores and fluid inclusions are often aligned perpendicular to the crystal growth surface. These features are related to the apatite crystallization from hydrothermal fluids (Chakhmouradian et al., 2017; Zheng et al., 2022). The LREE concentrations in apatite are lower than those of stage II calcite, possibly caused by the crystallization of calcite and monazite. Fractionation of REE-bearing minerals may have scavenged LREEs from the ore-forming fluids (Henderson, 1984). The Cl content of the Huayuan apatite is low (max 0.423%, avg. 0.085%), similar to that of typical hydrothermal apatite but lower than that of typical magmatic apatite (Cao et al., 2012; Chen et al., 2019). The Huayuan apatite also has high Mg content (max 0.44%, mean 0.03%, n = 90), which differs from that of typical magmatic and purely hydrothermal apatite (O'Sullivan et al., 2020). This may have resulted from the mixing of Mg-rich meteoric water with the hydrothermal ore fluids. The Mg was likely leached from the hanging-wall sequences *via* meteoric water seepage. Furthermore, the Fisher discriminant classification indicates that the Huayuan apatite is geochemically different from the apatite with magmatic or purely hydrothermal source (Figure 7). This also suggests that fluids from other sources may have involved in the mineralization, e.g., meteoric water. The Sr/Y ratio of the Huayuan apatite (3.20) is higher than that of magmatic-sourced apatite (~1.60; O'Sullivan et al., 2020). Meanwhile, REE concentrations of the Huayuan apatite also differ from the apatite with clastic origin. Furthermore, the mudstone wallrocks deposited in carbonate platform environment lacks clastics, as observed under the microscope.

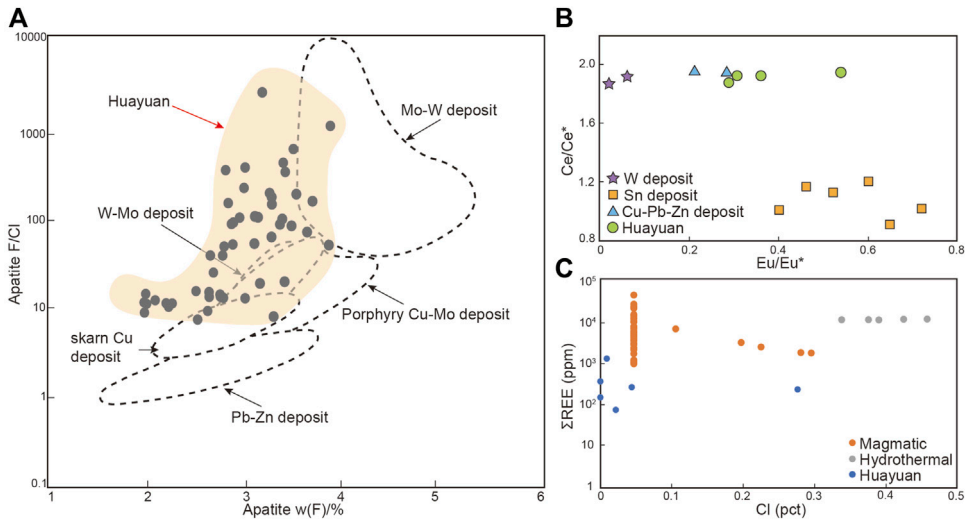

FIGURE 8
Plots of **(A)** F/Cl vs F (after Cao et al., 2012), **(B)** Ce/Ce* vs Eu/Eu* (after Ding et al., 2015), and **(C)** ΣREE vs Cl (data from O'Sullivan et al., 2020) for apatite from different types of deposits.

We suggest that our apatite samples have had a hydrothermal origin, because: 1) they are characterized by weakly negative Eu and weakly positive Ce anomalies, different from typical magmatic or sedimentary apatite (Gao et al., 2021); 2) they are slightly enriched in middle REEs (MREEs) but depleted in both LREEs and HREEs, similar to typical hydrothermal apatite (Chen et al., 2019); 3) they have low U concentration, high Th/U ratio, and coexist with ore-related pyrite; 4) they cut the diagenetic-related fissures; 5) they have high Mg but low Cl concentrations.

6.2 Characteristics of ore-forming fluids

Halogen compositions also vary among magmatic and hydrothermal ore-related apatite (Cao et al., 2012): Porphyry Mo-W ore-related apatite has the highest F content and F/Cl ratio; porphyry W-Mo and Cu-Mo ore-related apatite has lower F content and F/Cl ratio; skarn Cu and Pb-Zn ore-related apatite has the lowest F content and F/Cl ratio (Figure 8A). Due to the high and low solubility of Cl and F in aqueous solution, respectively (Brehler and Fuge, 1974), apatite associated with crustal melt is often F-rich and Cl-poor (Wang et al., 2014). The Huayuan apatite has mostly low F content and low F/Cl ratio (F > 1.8 wt%, Cl < 0.4 wt%), which are higher than the average values of apatite from the other Pb-Zn deposit types (Cao et al., 2012). This suggests material input from deep strata by the ore-forming fluids. Apatite is less susceptible to alteration, and would inherit the Sr and Y signature in the fluids (Pan et al., 2016). The Huayuan Pb-Zn ore fluids were interpreted to be water-rich, as supported by the high apatite Sr/Y ratio (Xing and Shu, 2021). Moreover, Sr isotopes of the Huayuan Pb-Zn ore fluid are higher than those of the LCQF limestone but lower than those of the deep strata (Wei et al., 2017), suggesting that the fluids may have reacted with the deep strata.

The apatite Mn, Eu, and Ce concentrations can indicate the magma redox state (Drake, 1975; Streck and Dilles, 1998; Sha and Chappell, 1999; Prowatke and Klemme, 2006; Cao et al., 2012; Miles et al., 2014; Pan et al., 2016; Xiong et al., 2017; Chen and Zhang, 2018; Xiong Y. et al., 2019; Xing et al., 2020). This is because Mn, Eu, and Ce have mainly two valence states, i.e., Mn^{4+} and Mn^{2+}, Eu^{3+} and Eu^{2+}, and Ce^{4+} and Ce^{3+}. Mn^{2+}, Eu^{3+}, and Ce^{3+} are more likely to replace Ca^{2+}in apatite (Shannon, 1976; Sha and Chappell, 1999; Belousova et al., 2002). When the fluid is oxidized, the proportions of Mn^{4+}, Eu^{3+}, Ce^{4+}, and Eu/Eu* in the fluid increase, whereas the Mn^{2+} and Ce/Ce* decrease, and *vice versa* when the fluid is reduced. The Huayuan apatite has negative Eu anomalies (wide Eu/Eu* range) and weakly positive Ce anomalies (Figure 8B), which is likely caused by redox changes. Moreover, the Huayuan apatite was formed during the main ore stage (stage II) when extensive thermochemical sulfate reduction (TSR) occurred (Wei et al., 2017), during which the ore-forming fluids have become more reducing. As the TSR proceeded, the Eu/Eu* ratio of the ore fluids (as thus their crystallizing apatite) decreased. The ore-fluid oxygen fugacity in the Huayuan Pb-Zn orefield was considered higher than that of typical Cu-Pb-Zn, W, and Sn deposits (Ding et al., 2015).

The apatite ΣREE (74—1,255 ppm) and Cl (< 0.42 ppm) concentrations of the Huayuan Pb-Zn orefield are significantly lower than those with magmatic and magmatic-hydrothermal origins (Figure 8C; O'Sullivan et al., 2020). In addition, the mineralization temperature of the Huayuan Pb-Zn deposits (140°C–328°C; Zhou et al., 2015) is lower than that of typical magmatic-related deposits but higher than that of typical MVT deposits (Xiong et al., 2020; Wu et al., 2021), indicating that the fluid origin was independent from magmatism. The mixing of various fluids may have resulted in the wide range of mineralization temperatures. Moreover, C-H-O isotope studies indicate that the Huayuan ore-forming fluids may include meteoric water. This is consistent with the apatite geochemical signatures that reflect the mixing of brine and meteoric water. In addition, The Fisher discriminant results also suggest that the Huayuan ore-forming fluids may have multiple sources. The Huayuan apatite has higher Mg content (max .44%, mean .03%, $n = 90$) than typical hydrothermal apatite (O'Sullivan et al., 2020), and the hanging-wall of the Huayuan Pb-Zn orebodies comprises Mg-rich dolomite. We thus suggest that the Mg may have been leached from the hanging-wall dolomite by the percolating meteoric water. The Mg-rich meteoric water may have then mixed with the hydrothermal fluid, passing the high Mg signature into the crystallizing apatite. Therefore, the Huayuan Pb-Zn ore fluids may have included brine and meteoric water

components, and are characterized by being F-rich, Cl- and REE-poor, and decreasing oxygen fugacity with the fluid evolution.

6.3 Metallogenic model

The Huayuan Pb-Zn orebodies are hosted in the platform-facies LCQF reef limestone, and structurally controlled by the Huayuan-Zhangjiajie fault zone. The geological and metallogenic characteristics of the Huayuan Pb-Zn orefield are comparable to typical Mississippi Valley-type (MVT) deposits (Leach et al., 2010; 2005; Yang and Lao, 2007; Zhou et al., 2015; Xiong S.-F. et al., 2019). In addition, the Huayuan Pb-Zn metallogeny was likely unaffected by magmatism (e.g., Zhou et al., 2014; Wu et al., 2021; Hu et al., 2022).

Previous studies showed that the sulfide Pb isotopes and sphalerite Zn isotopes of the Huayuan Pb-Zn ores are similar to those of the regional Proterozoic basement rocks (Zhou et al., 2016; Zhang et al., 2022), implying that the basement may have been a key metal source. In addition, the S isotopes of ore sulfides are similar to those of the LCQF limestone (e.g., Zhou et al., 2016; Wu et al., 2021), suggesting that the latter may have been a major ore sulfur source. The regional fault zones, notably the Huayuan-Zhangjiajie, controlled the distribution of Pb-Zn mineralization (Li et al., 2010). Therefore, the Caledonian orogenic event may have facilitated large-scale brine circulation and concentration in the Huayuan district (Wu et al., 2021). The circulating brine may have extracted the metals from the basement rocks, and transported them to the LCQF. The hydrothermal fluid may have mixed with meteoric water in the LCQF, which cooled and diluted the ore fluid and eventually led to ore deposition.

7 Conclusion

1) Apatite in the Huayuan orefield is of hydrothermal origin.
2) Ore-forming fluids in the Huayuan orefield may include brine and meteoric water. The fluids are characterized by being F-rich, Cl-poor, and REE-poor, with decreasing oxygen fugacity with the fluid evolution.
3) Metallogeny of the Huayuan Pb-Zn orefield was unlikely to be magmatic-related.

Data availability statement

The original contributions presented in the study are included in the article/Supplementary Material, further inquiries can be directed to the corresponding author.

Author contributions

R-CT, Y-JS, and Y-QX designed the experiment; R-CT, H-TW, J-KZ, and M-DY carried out the experiment; R-CT, Y-QX, and M-DY analyzed the data. R-CT wrote the manuscript.

Funding

This research was supported by the Open Topic of Hunan Key Laboratory of Land Resources Evaluation and Utilization (SYS-ZX-201905), the Hunan Innovation Team project (2021RC4055), the Hunan Key Research and Development program (2019SK2261), the Key Laboratory of Metallogenic Prediction of Non-ferrous Metals and Geological Environment Monitoring project (2021YSJS04), and the Hunan Academy of Geology (HNGSTP202105).

Acknowledgments

We thank the editor and reviewers for their constructive comments and suggestions.

Conflict of interest

The authors declare that the research was conducted in the absence of any commercial or financial relationships that could be construed as a potential conflict of interest.

Publisher's note

Supplementary material

The Supplementary Material for this article can be found online at: https://www.frontiersin.org/articles/10.3389/feart.2022.1083799/full#supplementary-material

References

Ayers, J. C., and Watson, E. B. (1993). Apatite/fluid partitioning of rare-Earth elements and strontium: Experimental results at 1.0 GPa and 1000°C and application to models of fluid-rock interaction. *Chem. Geol. Geochem. Accessory Minerals* 110, 299–314. doi:10.1016/0009-2541(93)90259-L

Barfod, G. H., Krogstad, E. J., Frei, R., and Albarède, F. (2005). Lu-Hf and PbSL geochronology of apatites from proterozoic terranes: A first look at Lu-Hf isotopic closure in metamorphic apatite. *Geochimica Cosmochimica Acta* 69, 1847–1859. doi:10.1016/j.gca.2004.09.014

Belousova, E. A., Griffin, W. L., O'Reilly, S. Y., and Fisher, N. I. (2002). Apatite as an indicator mineral for mineral exploration: Trace-element compositions and their relationship to host rock type. *J. Geochem. Explor.* 76, 45–69. doi:10.1016/S0375-6742(02)00204-2

Brehler, B., and Fuge, R. (1974). Chlorine. *Handb. Geochem.* 2, 213–297. doi:10.1007/978-3-642-65933-1_11

Cai, Y., Yang, H., Duan, R., Lu, S., Zhang, L., Liu, C., et al. (2014). Fluid inclusions and S, Pb, C isotope geochemistry of Pb-Zn deposits hosted by lower cambrian in western hunan-eastern Guizhou area. *Geoscience* 28, 29–41.

Cao, M., Li, G., Qin, K., Seitmuratova, E. Y., and Liu, Y. (2012). Major and trace element characteristics of apatites in granitoids from Central Kazakhstan: Implications for petrogenesis and mineralization. *Resour. Geol.* 62, 63–83. doi:10.1111/j.1751-3928.2011.00180.x

Chakhmouradian, A. R., Reguir, E. P., Zaitsev, A. N., Couëslan, C., Xu, C., Kynický, J., et al. (2017). Apatite in carbonatitic rocks: Compositional variation, zoning, element

partitioning and petrogenetic significance. *Lithos* 275, 188–213. doi:10.1016/j.lithos.2016.12.037

Charvet, J. (2013). The neoproterozoic–early paleozoic tectonic evolution of the South China Block: An overview. *J. Asian Earth Sci.* 74, 198–209. doi:10.1016/j.jseaes.2013.02.015

Chen, L., and Zhang, Y. (2018). *In situ* major-trace-elements and Sr-Nd isotopic compositions of apatite from the Luming porphyry Mo deposit, NE China: Constraints on the petrogenetic-metallogenic features. *Ore Geol. Rev.* 94, 93–103. doi:10.1016/j.oregeorev.2018.01.026

Chen, M., Bagas, L., Liao, X., Zhang, Z., and Li, Q. (2019). Hydrothermal apatite SIMS Th Pb dating: Constraints on the timing of low-temperature hydrothermal Au deposits in Nibao, SW China. *Lithos* 325, 418–428. doi:10.1016/j.lithos.2018.11.018

Chiang, L. H., Kotanchek, M. E., and Kordon, A. K. (2004). Fault diagnosis based on Fisher discriminant analysis and support vector machines. *Comput. Chem. Eng.* 28, 1389–1401. doi:10.1016/j.compchemeng.2003.10.002

Chiang, L. H., Russell, E. L., and Braatz, R. D. (2000). *Fault detection and diagnosis in industrial systems*. Heidelberg, Germany: Springer Science & Business Media.

Deng, J., Wang, C., Bagas, L., Carranza, E. J. M., and Lu, Y. (2015). Cretaceous–cenozoic tectonic history of the jiaojia fault and gold mineralization in the jiaodong peninsula, China: Constraints from zircon U–Pb, illite K–Ar, and apatite fission track thermochronometry. *Min. Deposita* 50, 987–1006. doi:10.1007/s00126-015-0584-1

Ding, T., Ma, D., Lu, J., and Zhang, R. (2015). Apatite in granitoids related to polymetallic mineral deposits in southeastern Hunan Province, Shi–Hang zone, China: Implications for petrogenesis and metallogenesis. *Ore Geol. Rev.* 69, 104–117. doi:10.1016/j.oregeorev.2015.02.004

Drake, M. J. (1975). The oxidation state of europium as an indicator of oxygen fugacity. *Geochimica Cosmochimica Acta* 39, 55–64. doi:10.1016/0016-7037(75)90184-2

Duan, Q., Cao, L., Zeng, J., Zhou, Y., Tang, Z., and Li, K. (2014). Rb-Sr dating of sphalerites from shizishan Pb-Zn deposit in huayuan ore concentration area, western hunan, and its geological significance. *Earth Sci.* 39, 977–999.

Duan, Q. (2014). *The research of the metallogenic regularity of stratabound zinc-lead deposits from sinian-cambrian in the western hunan and eestern hubei (ph. D.)*. Hubei, China: CUG.

Duda, R. O., and Hart, P. E. (1973). *Pattern classification and scene analysis*. New York, NY, USA: Wiley.

Edfelt, Å., Armstrong, R. N., Smith, M., and Martinsson, O. (2005). Alteration paragenesis and mineral chemistry of the Tjårrojåkka apatite–iron and Cu (-Au) occurrences, Kiruna area, northern Sweden. *Min. Deposita* 40, 409–434. doi:10.1007/s00126-005-0005-y

Fu, S. (2011). Discussion on formation rules of high-grade Pb-Zn ore in Western Hunan. *Nonferrous Met. Sect.* 63, 27–35.

Gao, L.-E., Zeng, L., Zhao, L., Gao, J., and Shang, Z. (2021). Behavior of apatite in granitic melts derived from partial melting of muscovite of metasedimentary sources. *China Geol.* 4, 44–55. doi:10.31035/cg2021009

Griffin, W. L., Powell, W. J., Pearson, N. J., and O'Reilly, Z. (2008). "Glitter: Data reduction software for laser ablation ICP-MS" in *Laser ablation-ICP-MS in the Earth Sciences*, 204–207.

Hassan, A. A., Termine, J. D., and Haynes, C. V. (1977). Mineralogical studies on bone apatite and their implications for radiocarbon dating. *Radiocarbon* 19, 364–374. doi:10.1017/S0033822200003684

Hastie, T., Tibshirani, R., Friedman, J. H., and Friedman, J. H. (2009). *The elements of statistical learning: Data mining, inference, and prediction*. New York, NY, USA: Springer.

Henderson, P. (1984). "Chapter 1 - general geochemical properties and abundances of the rare earth elements," in *Developments in Geochemistry, rare earth element Geochemistry*. Editor P. Henderson (Netherlands, Europe: Elsevier), 1–32. doi:10.1016/B978-0-444-42148-7.50006-X

Hu, L., Li, Y.-K., Wu, Z., Bai, Y., and Wang, A. (2019). Two metasomatic events recorded in apatite from the ore-hosting dolomite marble and implications for Genesis of the giant Bayan Obo REE deposit, Inner Mongolia, Northern China. *J. Asian Earth Sci.* 172, 56–65. doi:10.1016/j.jseaes.2018.08.022

Hu, Y., Ye, L., Huang, Z., Wei, C., Wu, T., Xiang, Z., et al. (2022). Genetic model for early Cambrian reef limestone-hosted Pb-Zn deposits in the world-class Huayuan orefield, South China: New insights from mineralogy, fluorite geochemistry and sulfides *in situ* S-Pb isotopes. *Ore Geol. Rev.* 141. doi:10.1016/j.oregeorev.2021.104682104682

Hughes, J. M., and Rakovan, J. (2018). "1. The crystal structure of apatite, Ca5(PO4)3(F,OH,Cl)," in *1. The crystal structure of apatite, Ca5(PO4)3(F,OH,Cl)* (Berlin, Germany: De Gruyter), 1–12. doi:10.1515/9781501509636-004

Kordian, S., Mokhtari, M. A. A., Kouhestani, H., and Veiseh, S. (2020). Geology, mineralogy, structure and texture, geochemistry and Genesis of the Golestan Abad iron oxide-apatite deposit (East of Zanjan). *J. Econ. Geol.* 12, 299–325. doi:10.22067/econg.v12i3.79628

Kusebauch, C., John, T., Whitehouse, M. J., Klemme, S., and Putnis, A. (2015). Distribution of halogens between fluid and apatite during fluid-mediated replacement processes. *Geochimica Cosmochimica Acta* 170, 225–246. doi:10.1016/j.gca.2015.08.023

Leach, David.L., Bradley, D. C., Huston, D., Pisarevsky, S. A., Taylor, R. D., and Gardoll, S. J. (2010). Sediment-hosted lead-zinc deposits in earth history. *Econ. Geol.* 105, 593–625. doi:10.2113/gsecongeo.105.3.593

Leach, D. L., Sangster, D. F., Kelley, K. D., Large, R. R., Garven, G., Allen, C. R., et al. (2005). Sediment-hosted lead-zinc deposits: A global perspective. *Econ. Geol. 100th Ann. Vol.*, 561–607. doi:10.5382/AV100.18

Li, K. (2018). *Metallogenic model and prediction of the carbonate-hosted Pb-Zn deposits in western hunan and eastern Guizhou province, South China*. Wuhan, China: China University of Geosciences.

Li, Z.-X., Li, X.-H., Wartho, J.-A., Clark, C., Li, W.-X., Zhang, C.-L., et al. (2010). Magmatic and metamorphic events during the early Paleozoic Wuyi-Yunkai orogeny, southeastern South China: New age constraints and pressure-temperature conditions. *GSA Bull.* 122, 772–793. doi:10.1130/B30021.1

Liu, W., Zheng, R., Li, Y., and Gao, L. (1999). Study of bitumen in the huayuan lead-zinc deposit organic geochemistry study of MVT lead-zinc deposit. *ACTA SEDIMENTOL. SIN.* 1, 19–23.

Liu, W., and Zheng, R. (1999). Research of fluid inclusion gas composititon in huayuan lead-zinc deposits——organic-mineralization study of MVT lead-zinc deposits(II). *ACTA SEDIMENTOL. SIN.* 1, 111–117.

McClellan, G. H., and Van Kauwenbergh, S. J. (1990). *Mineralogy of sedimentary apatites*, 52. London, UK: Geological Society, London, Special Publications, 23–31. doi:10.1144/GSL.SP.1990.052.01.03

Metcalfe, I. (2006). Palaeozoic and Mesozoic tectonic evolution and palaeogeography of East Asian crustal fragments: The Korean Peninsula in context. *Gondwana Res. Tect. Evol. Korean Peninsula Adjacent Crustal Fragm. Asia* 9, 24–46. doi:10.1016/j.gr.2005.04.002

Miles, A. J., Graham, C. M., Hawkesworth, C. J., Gillespie, M. R., Hinton, R. W., and Bromiley, G. D. (2014). Apatite: A new redox proxy for silicic magmas? *Geochimica Cosmochimica Acta* 132, 101–119. doi:10.1016/j.gca.2014.01.040

O'Sullivan, G., Chew, D., Kenny, G., Henrichs, I., and Mulligan, D. (2020). The trace element composition of apatite and its application to detrital provenance studies. *Earth-Science Rev.* 201. doi:10.1016/j.earscirev.2019.103044103044

Pan, L.-C., Hu, R.-Z., Wang, X.-S., Bi, X.-W., Zhu, J.-J., and Li, C. (2016). Apatite trace element and halogen compositions as petrogenetic-metallogenic indicators: Examples from four granite plutons in the Sanjiang region, SW China. *Lithos* 254 (255), 118–130. doi:10.1016/j.lithos.2016.03.010

Peng, G. (1986). A preliminary discussion on the origin of stratabound Lead-zine ore deposits in the Yutan region of Huayuan county, Hunan province. *Chin. J. Geol.* 2, 179–186.

Prokopyev, I. R., Doroshkevich, A. G., Ponomarchuk, A. V., and Sergeev, S. A. (2017). Mineralogy, age and Genesis of apatite-dolomite ores at the Seligdar apatite deposit (Central Aldan, Russia). *Ore Geol. Rev.* 81, 296–308. doi:10.1016/j.oregeorev.2016.10.012

Prowatke, S., and Klemme, S. (2006). Trace element partitioning between apatite and silicate melts. *Geochimica Cosmochimica Acta* 70, 4513–4527. doi:10.1016/j.gca.2006.06.162

Sha, L.-K., and Chappell, B. W. (1999). Apatite chemical composition, determined by electron microprobe and laser-ablation inductively coupled plasma mass spectrometry, as a probe into granite petrogenesis. *Geochimica Cosmochimica Acta* 63, 3861–3881. doi:10.1016/S0016-7037(99)00210-0

Shannon, R. D. (1976). Revised effective ionic radii and systematic studies of interatomic distances in halides and chalcogenides. *Acta Cryst. A* 32, 751–767. doi:10.1107/S0567739476001551

Shu, J. (1983). Preliminary discussion on the origin of Lead and Zinc-sulfide deposit in Yutang area. *Geotect. Metallogenia* 4, 309–320. doi:10.16539/j.ddgzyckx.1983.04.004

Streck, M. J., and Dilles, J. H. (1998). Sulfur evolution of oxidized arc magmas as recorded in apatite from a porphyry copper batholith. *Geology* 26, 523–526. doi:10.1130/0091-7613(1998)026<0523:SEOOAM>2.3

Sun, Y., Lin, W., and Zhou, Z. (1985). Algae fossil assemblage, sedimentary environment and mineralization of lower Cambrian Qingxudong formation, Yutang, Huayuan, Hunan. *J. Chengdu Coll. Geol.* 52, 60–112.

Tang, Z., Deng, F., Li, K., Duan, Q., Zou, X., and Dai, P. (2012). Stratigraphic characteristics of the cambrian Qingxudong Formation in relation to lead-zinc mineralization in Western hunan-eastern Guizhou area. *Geol. China* 39, 1034–1041.

Wang, H., Cai, K., Sun, M., Xia, X.-P., Lai, C.-K., Li, P., et al. (2022). Apatite as a magma redox indicator and its application in metallogenic research. *Lithos* 422. doi:10.1016/j.lithos.2022.106749106749

Wang, J., and Li, Z.-X. (2003). History of neoproterozoic rift basins in South China: Implications for rodinia break-up. *Precambrian Res. Precambrian Tect. East Asia relevance supercontintent Evol.* 122, 141–158. doi:10.1016/S0301-9268(02)00209-7

Wang, X.-S., Hu, R.-Z., Bi, X.-W., Leng, C.-B., Pan, L.-C., Zhu, J.-J., et al. (2014). Petrogenesis of late cretaceous I-type granites in the southern yidun terrane: New constraints on the late mesozoic tectonic evolution of the eastern Tibetan plateau. *Lithos* 209, 202–219. doi:10.1016/j.lithos.2014.08.016

Wei, H., Shao, Y., Ye, Z., Xiong, Y., Zhou, H., and Xie, Y. (2017). REE and Sr isotope geochemistry of gangue calcites from Huayuan Pb-Zn orefield in Western Hunan, China. *Chin. J. Nonferrous Metals* 27, 2329–2339. doi:10.19476/j.ysxb.1004.0609.2017.11.19

Wei, H., Xiao, K., Shao, Y., Kong, H., Zhang, S., Wang, K., et al. (2020). Modeling-based mineral system approach to prospectivity mapping of stratabound hydrothermal deposits: A case study of MVT Pb-Zn deposits in the huayuan area,

northwestern hunan province, China. *Ore Geol. Rev.* 120. doi:10.1016/j.oregeorev.2020.103368103368

Wu, T., Huang, Z., Ye, L., Wei, C., Chen, J., Yang, M., et al. (2021). Origin of the carbonate-hosted Danaopo Zn-Pb deposit in Western Hunan Province, China: Geology and *in-situ* mineral S-Pb isotope constraints. *Ore Geol. Rev.* 129. doi:10.1016/j.oregeorev.2020.103941103941

Xie, W. (1983). Lead sulfur isotopic Genesis geochemistry of some stratified lead-zinc deposits in Hunan Province. *Geol. Explor.* 10, 21–29.

Xing, K., and Shu, Q. (2021). Applications of apatite in study of ore deposits: A review. *Mineral. Deposits* 40, 189–205. doi:10.16111/j.0258-7106.2021.02.001

Xing, K., Shu, Q., Lentz, D. R., and Wang, F. (2020). Zircon and apatite geochemical constraints on the formation of the Huojihe porphyry Mo deposit in the Lesser Xing'an Range, NE China. *Am. Mineralogist* 105, 382–396. doi:10.2138/am-2020-7226

Xiong, S.-F., Jiang, S.-Y., Ma, Y., Liu, T., Zhao, K.-D., Jiang, M.-R., et al. (2019). Ore Genesis of Kongxigou and Nanmushu Zn-Pb deposits hosted in Neoproterozoic carbonates, Yangtze Block, SW China: Constraints from sulfide chemistry, fluid inclusions, and *in situ* S-Pb isotope analyses. *Precambrian Res.* 333. doi:10.1016/j.precamres.2019.105405105405

Xiong, Y., Shao, Y., Cheng, Y., and Jiang, S. (2017). Discrete jurassic and cretaceous mineralization events at the Xiangdong w(-sn) deposit, Nanling Range, South China. *Econ. Geol.* 115, 285–413. doi:10.5382/econgeo.4704

Xiong, Y., Shao, Y., Mao, J., Wu, S., Zhou, H., and Zheng, M. (2019). The polymetallic magmatic-hydrothermal Xiangdong and Dalong systems in the W–Sn–Cu–Pb–Zn–Ag Dengfuxian orefield, SE China: constraints from geology, fluid inclusions, H–O–S–Pb isotopes, and sphalerite Rb–Sr geochronology. *Miner. Deposita* 54, 1101–1124. doi:10.1007/s00126-019-00863-x

Xiong, Y. Q., Shao, Y. J., Zhou, H. D., Wu, Q. H., Liu, J. P., Wei, H. T., et al. (2020). Ore-forming mechanism of quartz-vein-type W-Sn deposits of the Xitian district in SE China: Implications from the trace element analysis of wolframite and investigation of fluid inclusions. *Ore Geol. Rev.* 83, 152–173. doi:10.1016/j.oregeorev.2016.12.007

Xu, L.-L., Bi, X.-W., Hu, R.-Z., Tang, Y.-Y., Wang, X.-S., Huang, M.-L., et al. (2019). Contrasting whole-rock and mineral compositions of ore-bearing (Tongchang) and ore-barren (Shilicun) granitic plutons in SW China: Implications for petrogenesis and ore Genesis. *Lithos* 337, 54–66. doi:10.1016/j.lithos.2019.03.031

Yang, S., Jiang, S., Mao, Q., Chen, Z., Rao, C., Li, Xiaoli, et al. (2022a). Electron probe microanalysis in Geosciences: Analytical procedures and recent advances. *At. Spectrosc.* 43, 186–200. doi:10.46770/AS.2021.912

Yang, S., and Lao, K. (2007). Geological characteristics and ore indicators of lead-zinc deposits in northwestern Hunan, China. *Geol. Bull. China* 7, 899–908. doi:10.3969/j.issn.1671-2552.2007.07.015

Yang, Z., Jiang, M., Zhao, S., Ding, Z., and He, M. (2022b). Stable isotopes and halogen geochemistry of the huayuan carbonate-hosted Pb-Zn ore district, South China: Implications for the salt source of ore-forming fluids. *Acta Geol. Sin. - Engl. Ed.* 96, 506–516. doi:10.1111/1755-6724.14857

Yao, W.-H., and Li, Z.-X. (2016). Tectonostratigraphic history of the ediacaran–silurian Nanhua foreland basin in South China. *Tectonophysics* 674, 31–51. doi:10.1016/j.tecto.2016.02.012

Zhang, R., and Yang, S. (2016). A mathematical model for determining carbon coating thickness and its application in electron probe microanalysis. *Microsc. Microanal.* 22, 1374–1380. doi:10.1017/S143192761601182X

Zhang, W.-D., Li, B., Lu, A.-H., Elatikpo, S. M., Chen, H., and Chen, X.-D. (2022). Origin of the Early Cambrian Huayuan carbonate-hosted Zn-Pb orefield, South China: Constraints from sulfide trace elements and sulfur isotopes. *Ore Geol. Rev.* 148. doi:10.1016/j.oregeorev.2022.105044105044

Zhao, J.-H., Zhou, M.-F., Yan, D.-P., Zheng, J.-P., and Li, J.-W. (2011). Reappraisal of the ages of neoproterozoic strata in South China: No connection with the grenvillian orogeny. *Geology* 39, 299–302. doi:10.1130/G31701.1

Zhao, S., Pan, W., Yang, S., Yin, T., Jiang, T., Tian, J., et al. (2016). Geological characteristics and genesis of lead-zinc deposits by lower cambrian in western hunan-northeastern Guizhou area. *Guizhou Geol.* 33, 257–264.

Zheng, J., Shen, P., and Feng, W. (2022). Hydrothermal apatite record of ore-forming processes in the Hatu orogenic gold deposit, West Junggar, Northwest China. *Contrib. Mineral. Pet.* 177, 27. doi:10.1007/s00410-022-01893-x

Zhou, H., Shao, Y., Ye, Z., and Wei, H. (2015). *Fluid inclusions investigation on the Danaopo lead-zinc deposit in Huayuan County*. Huayuan, China: western Hunan Province, SE China.

Zhou, J., Huang, Z., and Yan, Z. (2013). The origin of the Maozu carbonate-hosted Pb–Zn deposit, southwest China: Constrained by C–O–S–Pb isotopic compositions and Sm–Nd isotopic age. *J. Asian Earth Sci.* 73, 39–47. doi:10.1016/j.jseaes.2013.04.031

Zhou, Y., Duan, Q., Chen, Y., Tang, J., Cao, L., Peng, S., et al. (2016). C, O, H, S, Pb and Sr isotope constraints on the metals sources of huayuan Pb-Zn deposits in western hunan. *Acta Geol. Sin.* 90, 2786–2802.

Zhou, Y., Duan, Q., Tang, J., Cao, L., Li, F., Huang, H., et al. (2014). The large-scale low-temperature mineralization of lead-zinc deposits in western hunan-evidence from fluid inclusions. *Geol. Explor.* 50, 515–532. doi:10.13712/j.cnki.dzykt.2014.03.012

Zhou, Y., Duan, Q., Tang, J., Cao, L., Peng, S., and Gan, J. (2017). Carbon, hydrogen and oxygen isotopes of the Huayuan Pb-Zn ore deposit in Western Hu'nan Province and their implications for the source of ore-forming fluid. *Geol. Bull. China* 36, 823–833.

Zhou, Z., Wang, R., Zhuang, R., and Lao, K. (1983). The Genesis of huayuan-yutang lead-zinc deposit, hunan province. *J. Chengdu Coll. Geol.* 1, 19–116.

Zhu, X., Wang, Z., Huang, Y., and Wang, G. (2004). REE content and distribution in apatite and its geological tracing significance. *Chin. Rare Earths* 5, 41–63. doi:10.16533/j.cnki.15-1099/tf.2004.05.013